Dalton Transactions

ROYAL SOCIETY OF CHEMISTRY

PAPER

View Article Online
View Journal | View Issue

Cite this: *Dalton Trans.*, 2024, **53**, 10875

Synergistic reductive catalytic effects of an organic and inorganic hybrid covalent organic framework for hydrogen fuel production†

Sonia Rani,[a] Muhammad Nadeem,[b] Mazen R. Alrahili,[c] Marwan Shalash,[d] Moazzam H. Bhatti,[b] Khurram Shahzad Munawar,[e,f] Muhammad Tariq,*[a] Hafiz Muhammad Asif*[a] and Zeinhom M. El-Bahy[g]

Electrocatalytic hydrogen generation in alkaline medium has become widely used in a variety of sectors. However, the possibility for additional performance improvement is hampered by slow kinetics. Because of this restriction, careful control over processes such as water dissociation, hydroxyl desorption and hydrogen recombination is required. Covalent organic frameworks (COFs) based on porphyrin and polyoxometalates (POMs) show encouraging electrocatalytic performance, offering a viable route for effective and sustainable hydrogen generation. Their specific architectures lead to increased electrocatalytic activity, which makes them excellent choices for developing water electrolysis as a clean energy conversion method in the alkaline medium. In this regard, TTris@ZnPor and Lindqvist POM were coordinated to create a new eco-friendly and highly active covalent organic framework (TP@VL-COF). In order to describe TP@VL-COF, extensive structural and morphological investigations were carried out through FTIR, ^{1}H NMR, elemental analysis, SEM, fluorescence, UV-visible, PXRD, CV, N_2-adsorption isotherm, TGA and DSC analyses. In an alkaline medium, the electrocatalytic capability of 20%C/Pt, TTris@ZnPor, Lindqvist POM and TP@VL-COF was explored and compared for the hydrogen evolution reaction (HER). The TP@VL-COF showed the best catalytic efficiency for HER in an alkaline electrolyte, requiring just a 75 mV overpotential to drive 10 mA cm^{-2} and outperforming 20%C/Pt, TTris@ZnPor, Lindqvist POM and other reported catalysts. The Tafel slope value also indicates faster kinetics for TP@VL-COF (114 mV dec^{-1}) than for 20%C/Pt (182 mV dec^{-1}) TTris@ZnPor (116 mV dec^{-1}) and Lindqvist POM (125 mV dec^{-1}).

Received 15th March 2024,
Accepted 27th May 2024

DOI: 10.1039/d4dt00788c

rsc.li/dalton

1. Introduction

As the world's population rises and the economy develops, global energy consumption will rise steadily and predictably. Currently, fossil fuels such as natural gas, coal, and oil provide the majority of the energy we use.[1–3] Nonetheless, the depletion of these non-renewable resources, as well as the environmental adverse effects of their use, has prompted substantial research into advanced methods for capturing and storing clean and renewable energy, such as solar,[4] wind and water energy.[5–8] Due to its high energy density and zero pollutant emission, H_2 is expected to become a common fuel in many energy conversion devices in the near future.[9,10] Fuel cells,[11–13] water electrolysers, and rechargeable metal–air batteries are only a few examples of energy conversion devices based on electrocatalysis.[14–21] One of the most viable solutions to this energy issue is predicted to be the production of renewable H_2 energy in the presence of appropriate electrocatalysts.[22,23] The technique of electrochemical water splitting,[24,25] which is well-known for effectively producing hydrogen energy under moderate settings, has drawn a lot of interest and is currently regarded as an attractive approach to generate hydrogen fuel. The two semi-chemical cell processes used in this approach are the anode oxygen evolution reaction (OER)[26] and the cathode hydrogen evolution reaction (HER).[27,28] However, the sequential electron transfer, the slow kinetic phenomenon and the larger overpotential hinder the progress of the reaction.[29,30] Therefore, it becomes clear that

---

[a] *Inorganic Research Laboratory, Institute of Chemical Sciences, Bahauddin Zakariya University Multan, 60800, Pakistan. E-mail: drtariq2013@hotmail.com, hmasifc@bzu.edu.pk*
[b] *Department of Chemistry, Allama Iqbal Open University, Islamabad, Pakistan*
[c] *Physics Department, School of Science, Taibah University, Janadah Bin Umayyah Road, 42353 Medina, Saudi Arabia*
[d] *Department of Chemistry, College of Sciences and Arts Turaif, Northern Border University, Arar, Saudi Arabia*
[e] *Institute of Chemistry, University of Sargodha, 40100 Punjab, Pakistan*
[f] *Department of Chemistry, University of Mianwali, 42200 Punjab, Pakistan*
[g] *Department of Chemistry, Faculty of Science, Al-Azhar University, Nasar City11884, Cairo, Egypt*

† Electronic supplementary information (ESI) available. See DOI: **https://doi.org/10.1039/d4dt00788c**

efforts to create robust and effective electrocatalysts are essential to improve the efficiency of electrochemical hydrogen generation. Although Pt-based noble metal compounds[31,32] have been thoroughly investigated as state-of-the-art catalysts for HER, broad adoption of Pt/C in commercial applications poses major challenges.[33] This is mostly owing to the high cost of Pt and its susceptibility to dissolution and aggregation under poor operational circumstances. As a result, the resultant catalyst is costly and has poor electrocatalytic stability and activity.[34–36] Furthermore, the usual carbon support materials used for Pt and Pt-alloy catalysts are prone to corrosion on their surfaces due to electrochemical oxidation, resulting in the dissolution and aggregation of platinum nanoparticles.[37] Addressing the careful design of electrocatalysts remains a critical and unsolved job in order to overcome the inherent obstacles connected with both the metal catalyst and the carbon support.[38] Because of the special qualities, POMs, which contain non-noble metal sources, are frequently employed in electrocatalysis.[39–42] POMs and metalloporphyrins have been produced to construct supramolecular assemblies by electrostatic interactions or coordination.[43–46] These systems have been used as electrocatalytic reduction applications.[47,48] Yanyan Zhang and associates studied pseudo-pyridine-substituted Ni(II)-porphyrins and used them as catalysts for alkaline water splitting. The locations of pseudo-pyridine N-atoms are shown to be critical in controlling the microenvironment surrounding active sites, both in theoretical and experimental investigations. Pseudo-pyridine-substituted Ni(II)-porphyrins exhibit increased electrocatalytic activity as a result of this control, which affects the adsorption free energy of H-donating molecules through H-bonding interactions. With the lowest overpotential of 138 mV at 10 mA cm^{-2} for the HER, the electrocatalysts showed outstanding performance.[49] Furthermore, Xinyang Peng and colleagues created two copper complexes derived from porphyrin (designated as compounds 1 and 2) and evaluated their electrocatalytic activity in acetonitrile for the HER. By moving the catalytic wave to the anodic side by 190 mV, compound 1 was substantially more efficient than compound 2 for electrocatalytic HER. They had higher current densities with lower overpotentials.[50] Yuqin Dou and collaborators created POP (CoTAPP-CoTNPP), a nitrogen-rich azo-bridged metalated porphyrin, to improve the activity of the HER. The incorporation of cobalt porphyrins and azo groups improves the CoTAPP-CoTNPP HER performance by providing effective charge transfer efficiency and extended conjugated porous frameworks. Notably, CoTAPP-CoTNPP achieves a current density of 10 mA cm^{-2} with minimum overpotentials of 103 mV in acidic media and 170 mV in alkaline media.[51] Sifan Li and colleagues created polyoxometalate-modified Ag compounds 1 and 2. During the HER, these compounds are electrochemically restructured in 0.5 M H_2SO_4. The activated catalysts 1 and 2 exhibit strong electrocatalytic activity for the HER while maintaining remarkable long-term stability. Overpotentials of 112 mV (1) and 91 mV (2) are required to obtain a current density of 10 mA cm^{-2}, with matching Tafel slopes of 77 mV dec^{-1} and 65 mV dec^{-1}, respectively.[52] Porous materials have shown potential as efficient catalysts in comprehensive water splitting, including conjugated microporous polymers (CMPs),[53] metal–organic frameworks (MOFs)[54–56] and covalent organic frameworks (COFs).[57,58] COFs have become more and more popular in energy storage[59,60] and water splitting catalysis[61,62] because of their exceptional properties, including structural regularity, large surface area, porosity and diverse functionality. Shengsheng Cui *et al.* reported that when mesoporous polymers are coupled with Cu-porphyrin, they can form N-enriched carbon nanomaterials with a tubular structure and a large surface area. These materials contain either Cu or CuO, making them suitable for both the OER, which requires an overpotential of 350 mV to achieve 1.0 mA cm^{-2} and 450 mV to achieve 10 mA cm^{-2}, and the HER, which requires an overpotential of 190 mV to achieve 1.0 mA cm^{-2}.[63] So, electrocatalysts are required that overcome problems like large overpotentials,[64–66] lower stability, expensiveness,[67,68] and slow reaction kinetics.[69–72] The pH of the electrolyte solution (acidic or basic) can affect the reaction kinetics and the overall process efficiency.[73] Generally, the HER is more suited to maintain high current density in acidic electrolytes and is crucial in alkaline medium.[74–77] It is commonly acknowledged that the ease of electrooxidation of organic compounds in an alkaline solution is substantially greater than in an acidic one. The effect of poisoning is much reduced in this medium, and even platinum-based catalysts may not be required, allowing for the use of more cost-effective alternatives.[78,79]

As part of recent efforts, we have synthesized a new covalent organic framework, TP@VL-COF, as shown in Fig. 1, which comprises tetra-functionalized porphyrin possessing multiple hydroxyl groups located at the terminal positions of the porphyrin and vanadium-containing Lindqvist POM. An extensive structural and morphological analysis of the TP@VL-COF was carried out. After that, its electrocatalytic efficiency for HER

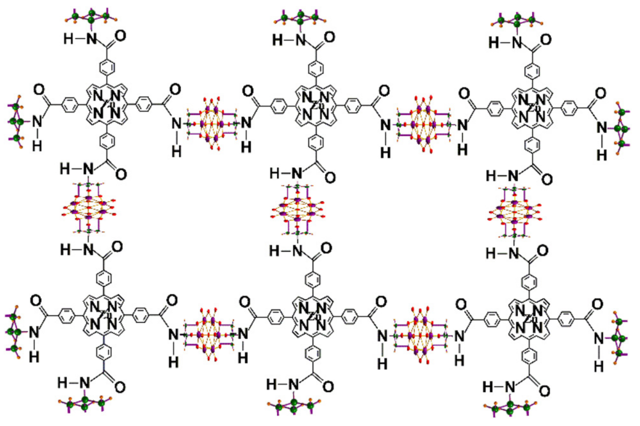

Fig. 1 Diagram of the TP@VL-COF comprising vanadium-containing Lindqvist POM and tetra-functionalized porphyrin. Colour codes: V = purple, H = orange, C = green and O = red. The reaction pathway is presented in Scheme S1.†

activity in alkaline medium was assessed. In order to accomplish a variety of electrocatalytic applications, this work presents a simple strategy for the systematic design of electrocatalysts.

2. Instrumentation and measurements

2.1. Chemicals and reagents

Lindqvist POM[80,81] and TTris@ZnPor[82] were synthesized according to the reported research. All of the chemicals and solvents were purchased from Merck and Macklin companies and utilized without additional modification.

2.2. Instruments and techniques

The electronic vibrations in TP@VL-COF were studied using a Shimadzu UV-1800 spectrophotometer, which was used to collect the UV-visible spectra in this study. Fourier transform infrared spectra were obtained using an FTIR spectrophotometer (8400-shimadzu) at room temperature with a KBr pellet within the 4000–400 cm^{-1} range in order to investigate functional groups at specific wave numbers. Solid sample ^1H NMR spectra were recorded using a Bruker spectrometer (AV-400) with a CP-MAS broadband probe of 4 mm diameter with MAS spinning speed $\geq$ 12 kHz at room temperature. By using various combinations of eluents with appropriate polarity, column chromatography (CC) and thin layer chromatography (TLC) using F-254 silica gel with a 20 × 20 cm^2 TLC plate size were employed to separate the generated porphyrin precursors from impurities. The F-7000 FL-spectrophotometer was used to record the fluorescence spectrum with a 5 nm (excitation and emission) wavelength slit at 400 PMT voltage. Using a Trios V5.5.1.5 (SDT650), thermogravimetric analysis (TGA) and differential scanning calorimetry (DSC) were carried out at a heating rate of 10 °C min^{-1} in a nitrogen environment. The measurement of nitrogen adsorption isotherms at 77 K was conducted using the Autosorb-iQ version 5.21 (Station-1) from Quantachrome. Cyclic voltammetry (CV) was performed by immersing the sample in a small amount of HNO_3 and then adding CH_3CN/DMF solution at room temperature with 10 mV s^{-1} scan rate in a nitrogen atmosphere using an electrochemical analyser (CH1660B). The supporting electrolyte was TBAP (tetrabutylammonium perchlorate) solution with a three-electrode system. The supporting electrolyte was a 0.1 M solution of KOH. Using the Bragg–Brentano geometry (Cu–K = 1.54056) and the Rigaku Miniflex 600 diffractometer, the PXRD pattern was recorded. An FEI-Quanta 3D FEG scanning electron microscope with a working distance of 10.0 mm and an accelerating voltage of 15 kV was used to obtain the SEM images for morphological analysis. The EuroEA elemental analyser was used in an elemental analysis investigation to determine the proportion of several elements such as carbon, hydrogen and nitrogen. All electrochemical (HER) studies were performed on the OrigaFlex OGF05A from Origalys coupled with the Rotating Disk Electrode OrigaTrod. A triple electrode system was employed, consisting of a counter electrode (carbon rod), a reference electrode (Ag/AgCl) and Ni foam modified electrodes with PCF/PCFN loaded ink as the working electrode (of TP@VL-COF) in 1 M KOH electrolyte.

2.3. Synthesis of TP@VL-COF

Lindqvist POM[80,81] (0.3 g, 4 eq.) and TTris@ZnPor[82] (0.07 g, 1 eq.) (ESI†) were added together in a small three-neck round-bottom flask containing dry dimethyl acetamide (DMAc) (2 to 3 ml). The mixture was heated at 85 °C with continuous stirring for 48 hours in a nitrogen environment. Using aluminium foil, the reaction mixture was shielded from light. Later, the mixture was transferred into a Teflon-coated autoclave and heated for 48 hours at 120 °C in an oven. The synthesized mixture was then cooled at room temperature and added drop by drop in 100 ml of cooled distilled water. After centrifugation and drying, the resultant product was washed with DMF, THF and hexane (3 times for 24 hours each). The dark purple coloured product was then dried in a vacuum to yield 70% of TP@VL-COF (based on porphyrin).

Elemental analysis (%) calcd for$\{[N(C_4H_9)_4]_3V_6O_{13}\}_4\{HNC(CH_2O)_3\}_4\{(CO)_4C_{44}H_{24}N_4Zn\}$ (FW = 4996.06); C 53.88, N 3.9, H 8.87; observed; C 53.32, N 3.47, H 8.53. ^1H NMR (400 MHz; DMSO.d$_6$): δ = 7.51–9.33 ppm [All $TBA^+([Bu_4N]^+)$, H]. FT-IR (KBr): ν_{max} = 3649, 3511 ($\nu_{N–H}$, m, br), 2964, 2935, 2874 ($\nu_{TBA^+([Bu4N]^+)}$), 1637 ($\nu_{C=O}$, vs), 879 ($\nu_{N–Zn}$, m, br), 1577–1458(s), 1396(sh), 1072(m), 1001(s) cm^{-1}. UV-vis spectrum (λ_{max} (nm) in DMF/CH_3CN (v/v = 1 : 1)): 430, 563 and 604 nm. CV = 1.44, 1.55, 1.7 and 2.34 V [oxidation potential], −0.87, −1.04, −1.15 and −1.38 V [reduction potential].

2.4. Procedure for the electrocatalytic HER setup

Electrocatalytic application for HER was performed utilizing a three-electrode setup. 5 mg of the catalyst, 1 mL of deionized water, 250 μL of isopropanol, and 25 μL of Nafion (D-521) were mixed to make a slurry for the working electrode. For four hours, the mixture was ultrasonicated to create a uniform ink. A Ni-foam substrate with a surface area of 1 cm^2 was evenly covered with 20 μL of this ink. In order to remove nickel oxide, all electrode substrates were first etched in 3 M HCl for three hours to create the Ni-foam electrodes. The electrodes were etched and then successively cleaned with ethanol, deionized water, and acetone. For linear sweep voltammetry (LSV) in a 1 M KOH electrolyte, a triple electrode system was used. It consisted of a carbon rod, Ag/AgCl and Ni-foam modified electrodes (TTris@ZnPor and TP@VL-COF each time) with PCF/PCFN-loaded ink as counter, reference and working electrodes, respectively. Standard 20%C/Pt electrodes were used for the HER, in contrast to TTris@ZnPor and TP@VL-COF.

3. Results and discussion

Elemental analysis was done to determine the percentages of carbon, hydrogen and nitrogen in TP@VL-COF. The observed values were 53.32%, 8.53% and 3.47% for C, H and N, respectively, as shown in Fig. S1(C).† To determine the essential functional groups, FT-IR analysis of TTris@ZnPor, TP@VL-COF and Lindqvist POM was conducted. IR peaks were noted for various assignments, as shown in Fig. 2(a), and all pertinent data are given in Table S1.† From the FT-IR study, the presence of TBA$^+$([Bu$_4$N]$^+$) in Lindqvist POM and TP@VL-COF was confirmed after observing the peaks at [2966, 2933, 2874] cm^{-1} and [2964, 2935, 2874] cm^{-1}, respectively. For the TP@VL-COF, the organic linker (C=O) peak was observed at 1637 cm^{-1}. The vibrational peak of the C–O group for TTris@ZnPor was observed at 1053 cm^{-1} prior to contact with Lindqvist POMs, and after interaction, in the TP@VL-COF, this peak was seen at 1072 cm^{-1}. According to Fig. 2(a) and Table S1,† the stretching bands for the (V=O)[81] and (V–O–V)[83] groups were found at wavenumbers of (970, 890) cm^{-1} and (721, 751) cm^{-1}, respectively. FT-IR measurements verified the covalent linkage between TTris@ZnPor and the Lindqvist POM in the TP@VL-COF.[84,85] UV-visible spectroscopy was performed to study the absorption bands of TTris@ZnPor, TP@VL-COF and Lindqvist POM as shown in Fig. 2(b) and the data are presented in Table S2.† The TP@VL-COF showed a strong Soret band at 430 nm attributed to the S$_0$ → S$_2$ electronic transition (π → π*) and a number of Q-bands at 563 nm and 604 nm owing to S$_0$ → S$_1$ electronic transitions, also indicating the formation of metalloporphyrin. There is not much difference in the absorption bands of TTris@ZnPor and TP@VL-COF except for reduced intensities of Soret and Q bands which verified that in the ground state no stronger electronic interactions could be observed between Lindqvist POM and TTris@ZnPor.[81,86] The ^{1}H NMR spectra for TP@VL-COF were carefully recorded and examined, revealing all significant and split signals with reasonable allocation. Fig. 2(c) displays the ^{1}H NMR spectra for TP@VL-COF. Signals at 7.51 ppm to 8.41 ppm in the ^{1}H NMR spectra of TP@VL-COF were used to identify the interior and outer aromatic phenyl ring protons represented as c and g. The peaks at 8.63, 8.92, 9.28 and

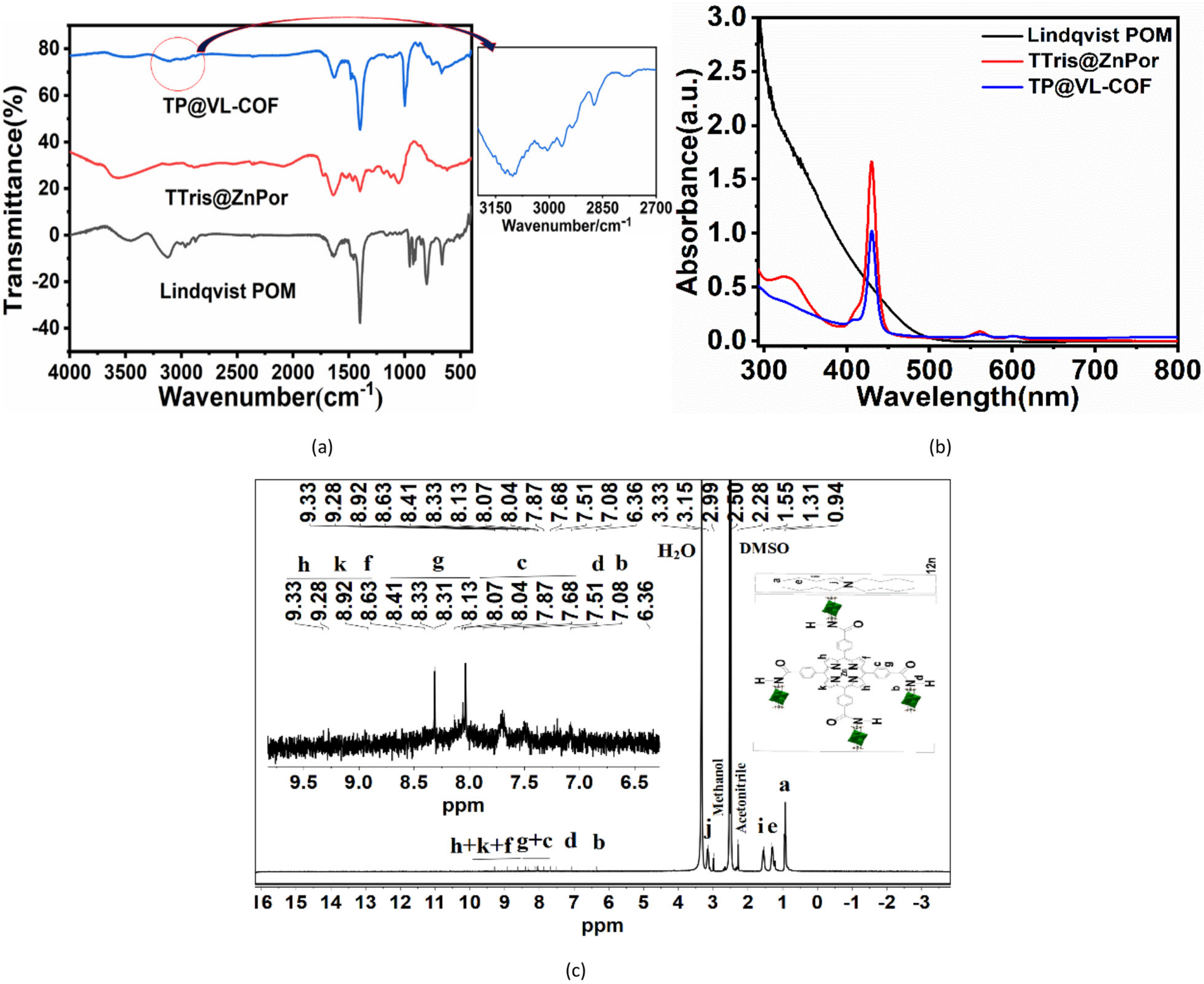

(a) (b)

(c)

Fig. 2 (a) Fourier transform infrared spectroscopic (FT-IR) spectra of the TP@VL-COF, TTris@ZnPor and Lindqvist POM. The zoomed-in portion shows the presence of TBA$^+$ peaks in the TP@VL-COF. (b) UV-vis electronic spectra of TTris@ZnPor, TP@VL-COF and Lindqvist POM. (c) ^{1}H NMR spectra of the TP@VL-COF.

9.33 ppm revealed pyrrole protons denoted as f, k, and h, respectively. No peak is observed at −3 ppm for core NH protons which confirms the attachment of zinc metal within the core of porphyrin.[87–89] The confirmation of the –NH group in the TP@VL-COF was done from downfield signals at 7.24 ppm. The –NH group is linker between TTris@ZnPor and Lindqvist POM for covalent linkage.[89,90] The presence of $TBA^+([Bu_4N])^+$ signals in TP@VL-COF was found at 0.94, 1.31, 1.55 and 3.15 ppm.[83] A signal of the $-CH_2$ group was observed at 6.36 ppm in TP@VL-COF.[81,91]

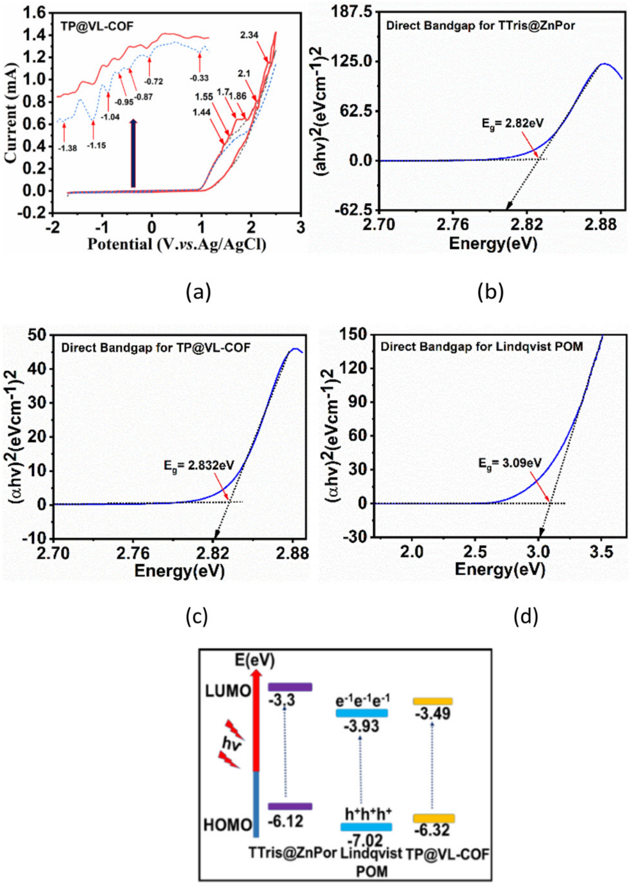

(a) (b)

(c) (d)

(e)

Fig. 3 (a) Cyclic voltammograms of the TP@VL-COF in DMF/CH_3CN (v/v = 1 : 1). The supporting electrolyte was TBAP. The zoomed-in portion on the right side of the graph indicates the reduction potential of the TP@VL-COF. The bandgap energy (E_g) evaluated through the Tauc plots of (b) TTris@ZnPor, (c) TP@VL-COF and (d) Lindqvist POM. (e) HOMO–LUMO band gaps of TTris@ZnPor, Lindqvist POM and TP@VL-COF.

Cyclic voltammetry (CV) was performed for electrochemical studies for TP@VL-COF in comparison with (Fc^+/Fc) as an internal standard electrode as shown in Fig. 3(a) and Fig. S1(a and b)† and the results are presented in Table 1. In CV measurements, the redox processes for the porphyrinic conjugated (π-ring) portion of the TP@VL-COF were detected because of the formation of radical anions and cations. After the attachment of Lindqvist POM with TTris@ZnPor, $V^{(V)}$ was oxidized into $V^{(VI)}$ with the resultant oxidation potential values of 1.86 V and 2.1 V and simultaneosly $V^{(VI)}$ was reduced to $V^{(V)}$ with the corresponding reduction potential values of about −0.33, −0.72 and −0.95 V, presenting the disproportionate reaction of vanadium ions ($V^{(VI)}$ and $V^{(V)}$) with one-electron transfer, as mentioned in Table 1.[86,92] In eqn (1) and (2), the onset value of E_{red} for TTris@ZnPor and TP@VL-COF was utilized to calculate the energy of the LUMO (lowest unoccupied molecular orbital) and HOMO (highest occupied molecular orbital).

$$\mathrm{LUMO} = -[E_{\mathrm{red}} - E_{1/2}\ (\mathrm{Fc/Fc^+}) + 4.8] \tag{1}$$

$$\mathrm{HOMO} = \mathrm{LUMO} - E_g \tag{2}$$

where $E_{1/2}$ (Fc/Fc^+) indicates the half-wave potential of ferrocene calculated using eqn (3).[93]

$$E_{1/2}\ (\mathrm{Fc/Fc^+}) = E_{\mathrm{oxi}} + E_{\mathrm{red}}/2 \tag{3}$$

E_g represents the optical band gap obtained through the Tauc plot as shown in Fig. 3(b–d). According to calculations using the above equations, TTris@ZnPor and Lindqvist POM have larger band gaps than TP@VL-COF. When TTris@ZnPor was irradiated with light of different wavelengths in a photoreactor, electron excitation was easy from the HOMO level to the LUMO level. The covalent attachment of TTris@ZnPor to Lindqvist POM decreased the LUMO level energy for TP@VL-COF, which induced electron transfer from TTris@ZnPor to Lindqvist POM and improved the photo-catalytic ability of the polymer, as shown in Fig. 3(e), and the data are presented in Table S3.† Similar results for the bandgap energy (E_g) were obtained from experimental (CV) and theoretically calculated (Tauc plot) data, resulting in a band gap (E_g) of 2.832 eV for TP@VL-COF, confirming the effectiveness of the experimental approach for the TP@VL-COF catalyst, as shown in Fig. 3(b–d).

Table 1 The redox (oxidation as well as reduction) potentials of TTris@ZnPor, TP@VL-COF, and Lindqvist POM determined by plotting current *vs.* potential using Ag/AgCl as a reference electrode through cyclic voltammetry

Compounds	Reduction					Oxidation				
	$V^{VI/V}$	$E_{red\ 1}$	$E_{red\ 2}$	$E_{red\ 3}$	$E_{red\ 4}$	$V^{V/VI}$	E_{ox1}	E_{ox2}	E_{ox3}	E_{ox4}
TTris@ZnPor	—	−1.14	0.86	—	—	—	0.79	0.99	1.32	—
TP@VL-COF	−0.33, −0.72, −0.95	−0.87	−1.04	−1.15	−1.38	1.86, 2.1	1.44	1.55	1.7	2.34
Lindqvist POM[86]	−0.43	—	—	—	—	−0.36	—	—	—	—

The thermogram of TP@VL-COF under a N_2 atmosphere displayed surprisingly remarkable thermal stability, indicating its applicability in high-temperature situations, as shown in Fig. 4(a). TP@VL-COF, in particular, showed a four-step weight loss pattern. The desorption of surface-adsorbed water molecules and tiny molecules within the material's pores accounts for roughly 3% of the mass loss from 33 °C to 178 °C. The second weight loss, which occurs from 184 °C to 285 °C and accounts for approximately 10% of the total weight loss, is caused by the disintegration of organic components inside the covalent organic framework. The third stage, which occurs between 288 °C and 349 °C and results in a 20% weight loss, is related to the loss of the inorganic portion inside the framework. Finally, the fourth stage, which occurs between 503 °C and 889 °C and accounts for approximately 12% of the total weight loss, is related to the loss of metallic parts inside the framework. Overall, the approximate weight loss was 45%.[94–96] Differential scanning calorimetry (DSC) was used to investigate the phase transition and thermal properties for TP@VL-COF, as shown in Fig. 4(b). At 231 °C, a glass transition was detected. The DSC study revealed heat absorption during transitions, at transition temperatures of 230 °C and 682 °C, indicating the breakdown point of the frameworks. Oxidation occurs at 765 °C and again decomposition starts. Moreover, the enthalpy change during this procedure was 1906.4 J g^{-1}.

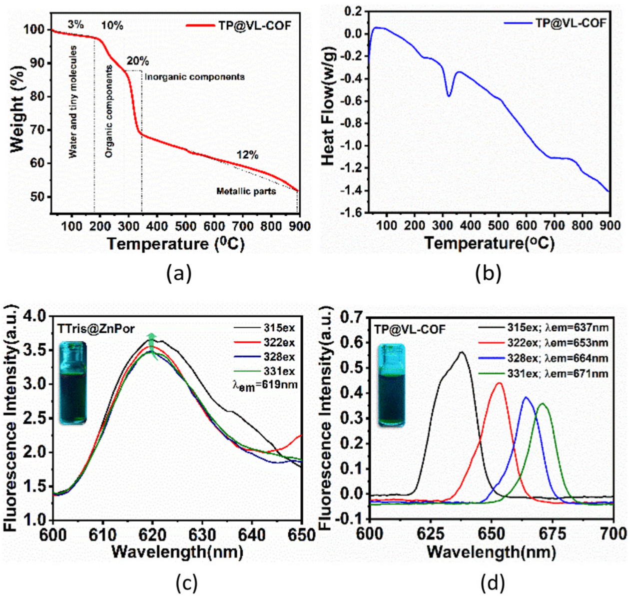

(a) (b)

(c) (d)

Fig. 4 (a) Thermogravimetric analysis (TGA) and (b) differential scanning calorimetery (DSC) for the TP@VL-COF at 10 °C min^{-1} heating rate under a N_2 atmosphere (0–900 °C temperature range). The fluorescence emission spectrum was measured at λ_{315}, λ_{322}, λ_{328} and λ_{331} nm excitation wavelengths for (c) TTris@ZnPor and (d) TP@VL-COF. The photograph was taken under a UV lamp by immersing the sample in HNO_3 and then adding a small amount of DMF.

The emission spectra of TTris@ZnPor and TP@VL-COF were investigated by fluorescence studies, as shown in Fig. 4(c and d). This was done without using any additional accessory. Place a small amount of the solid sample between two quartz slides and tape the slides together using cellotape. Place this sample at the centre of the fluorescence cuvette holder and rotate/translate the slide to get a good signal-to-noise ratio. In case the Stokes shift of the sample is small, extra precautions may be necessary to minimize the secondary inner filter effect. Fluorescence is actually the emission of photons during molecular relaxation from electrically excited states. Transitions between the electronic and vibrational levels of fluorescent molecules called polyatomic fluorophores are involved in the photonic activities that cause fluorescence.[97] Fluorescence emission tests were carried out with several excitation wavelengths (λ_{315}, λ_{322}, λ_{328} and λ_{331}) for both TTris@ZnPor and TP@VL-COF. For TTris@ZnPor, the emission wavelength (λ_{em}) was obtained at 619 nm, while for TP@VL-COF, the λ_{em} values were attained at 637, 653, 664 and 671 nm for λ_{315}, λ_{322}, λ_{328} and $\lambda_{331,}$ respectively. Furthermore, both TTris@ZnPor and TP@VL-COF exhibited fluorescence intensities at λ_{315}, λ_{322}, λ_{328} and λ_{331} of 3.67, 3.57, 3.49 and 3.47 a.u. and 0.56, 0.44, 0.39, and 0.36 a.u., respectively. The fluorescence intensity decreased in TP@VL-COF when Lindqvist POM was added. In particular, compared to TTris@ZnPor, the fluorescence intensity dropped by 15% for TP@VL-COF. The fluorescence quenching power of Lindqvist POM was responsible for the notable decrease in fluorescence intensity in TP@VL-COF, which showed that TP@VL-COF was formed by covalent bonding between TTris@ZnPor and Lindqvist POM because direct contact or close proximity between molecules is usually required for fluorescence quenching. So, our results strongly suggest that TTris@ZnPor and Lindqvist POM form a covalent bond during the synthesis of TP@VL-COF. The observed quenching of fluorescence further indicated a preferential photoinduced transfer of electrons from functionalized porphyrin to the POM.[88] Additionally, the increase in molecular collisions reduces the fluorescence intensity.[98–101] It was also observed that the effect of excitation wavelength on TP@VL-COF's fluorescence spectra was different from that for TTris@ZnPor.

As the excitation wavelength increased, we observed a decrease and red shift in the intensity of the fluorescence band in TP@VL-COF. Because excited electrons in traditional fluorophores settle down to the band edge before fluorescence, regardless of their initial excitation energy, the maximum photoluminescence remains constant for a given range of excitation wavelengths. It has been shown that in extremely stiff environments, such as viscous polymers, membranes, glasses and proteins, there are small changes that are dependent on the excitation wavelength.[102,103] The quantification of fluorescence quantum yield (QY) was performed for TTris@ZnPor and TP@VL-COF. Fluorescence and UV/visible absorption measurements were used for the calculation of the QY. For comparison, fluorescein in DMSO, a standard reference solution with a QY of about 0.98, was used. The following comparison formula approach was used to calculate the fluorescence quantum yield (QY):

$$Q_{\mathrm{Y.U}} = Q_{\mathrm{Y.R}} \times \frac{m_{\mathrm{U}}}{m_{\mathrm{R}}} \times \frac{{\eta_{\mathrm{U}}}^2}{{\eta_{\mathrm{R}}}^2} \tag{4}$$

The formula uses the following notations: 'U' in $\mathrm{Q_{Y.U}}$ stands for the unknown samples (TTris@ZnPor and TP@VL-COF), '$\mathrm{Q_{Y.R}}$' for the standard reference's quantum yield, and '*m*' for the slope obtained from the linear fit graph of UV absorption *vs.* integrated area for the specimens and the reference solution's fluorescence data. The refractive index is eliminated when the solvents used in the specimen and standard are the same. As a result, the computed quantum yield values for TTris@ZnPor and TP@VL-COF were 0.05 and 0.02, respectively.[104,105]

The crystalline properties of TP@VL-COF have been shown by the given powder X-ray diffraction (PXRD) spectrum (Fig. 5(a)).[106–110] From PXRD data, the calculated crystalline percentage was about 75% as mentioned in Table S5.† The crystal size (D) computed using the W–H plot for TP@VL-COF was found to be 14.45 nm and the resulting strain (ε) value from the linear fit graph was 0.00177. All relevant data are collected in Table S4.† The crystal size (D) was determined using eqn (5) and the W–H (Williamson–Hall) plot.

$$D = K\lambda/c \tag{5}$$

The specific surface area and porosity of TP@VL-COF were analysed using BET measurements obtained from the nitrogen adsorption isotherm at 77 K, as shown in Fig. 5(b). TP@VL-COF exhibited a type-IV isotherm curve, which is typical of mesoporous materials. The BET specific surface area of TP@VL-COF was 80.22 $\mathrm{m^2\ g^{-1}}$, with a total pore volume of 0.06 $\mathrm{cm^3\ g^{-1}}$.[94] The pore size of TP@VL-COF was 8.72 nm, which was determined from the pore size distribution (PSD) curve using non-local density functional theory (NLDFT) as shown in Fig. S3.†

The morphology of TP@VL-COF was confirmed by scanning electron microscopy (SEM), as shown in Fig. 6(a and b). SEM images confirmed the polymer nature of the TP@VL-COF formed. From SEM images, it has been observed that TP@VL-COF has a regularly distributed crystalline polymeric shape and has adopted a rod like morphology. This COF had a height of 3.7795 nm.[111]

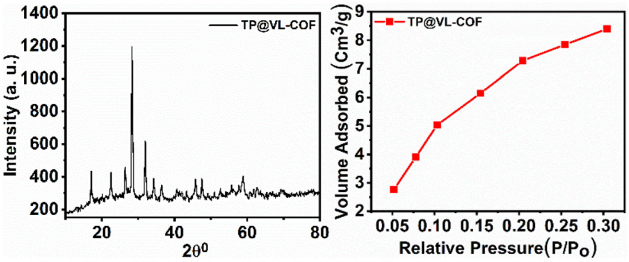

(a) (b)

Fig. 5 (a) Powder X-ray diffraction (PXRD) spectrum of the TP@VL-COF. (b) BET N_2-adsorption isotherm of the TP@VL-COF at 77 K.

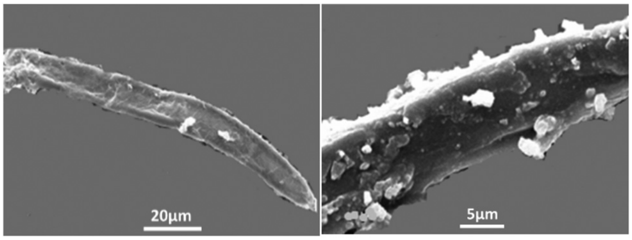

(a) (b)

Fig. 6 Scanning electron microscopy (SEM) images at (a) 20 μm and (b) 5 μm scales, showing the polymeric morphology of the TP@VL-COF (accelerating voltage = 10 kV).

4. Electrocatalytic HER studies

TTris@ZnPor and TP@VL-COF were assessed for their electrocatalytic properties utilizing a three-electrode setup for the HER. The formula ($E_{\mathrm{RHE}} = E_{\mathrm{Ag/AgCl}} + 0.059\ \mathrm{pH} + 0.197\ \mathrm{V}$) was used to convert the potential *vs.* Ag/AgCl to a potential *vs.* reversible hydrogen electrode (RHE). At a current density of 10 mA $\mathrm{cm^{-2}}$, the overpotential (η) was determined using the formula ($\eta_{\mathrm{HER}} = E_{\mathrm{RHE}}$) for HER. At a scan rate of 10 mV $\mathrm{s^{-1}}$, the potential range for the HER was changed from −0.5 to −1.5 V against Ag/AgCl. To find the overpotential of 20%C/Pt, TTris@ZnPor, Lindqvist POM and TP@VL-COF in an alkaline electrolyte, LSV was utilized. Cathodic LSV curves showed that 20%C/Pt, Lindqvist POM and TTris@ZnPor exhibited an overpotential of 113 mV, 105 mV and 146 mV, respectively, which are greater than that of TP@VL-COF of 75 mV at a current density of 10 mA $\mathrm{cm^{-2}}$, as shown in Fig. 7(a) and S4(a)† and described in Table 2. However, by obtaining the Tafel slope from the LSV data and plotting a graph between log (mA $\mathrm{cm^{-2}}$) and the overpotential, the reaction kinetics of 20%C/Pt, TTris@ZnPor, Lindqvist POM and TP@VL-COF was examined. So, TP@VL-COF exhibited the best overpotential and the smallest Tafel slope compared to the noble metal 20%C/Pt electrode. In order to indicate the rate-controlling step for the HER process, the Tafel slope is essential. The Tafel slopes of 20%C/Pt, Lindqvist POM and TTris@ZnPor were measured to be 182, 125 and 116 mV $\mathrm{dec^{-1}}$, respectively, which are higher than that of the TP@VL-COF of about 114 mV $\mathrm{dec^{-1}}$, as shown in Fig. 7(b) and S4(b).† These results demonstrated that in comparison to the 20%C/Pt, Lindqvist POM, and TTris@ZnPor, the TP@VL-COF has a smaller Tafel slope value, suggesting faster and more efficient HER kinetics (Table 2). The charge transfer resistance (R_{ct}) across the catalysts and electrolyte surface during the catalytic activity is shown by the diameter of the Nyquist plot. The Nyquist plots are shown in Fig. 7(c and d), where the semicircles for TTris@ZnPor and TP@VL-COF are clearly visible. The semicircles represent the charge transfer resistance of the electrode materials, and the semicircle's radius serves as a gauge for this resistance. TP@VL-COF, in particular, showed a much lower radius than TTris@ZnPor. The Lindqvist POM coordination facilitates the charge transfer,

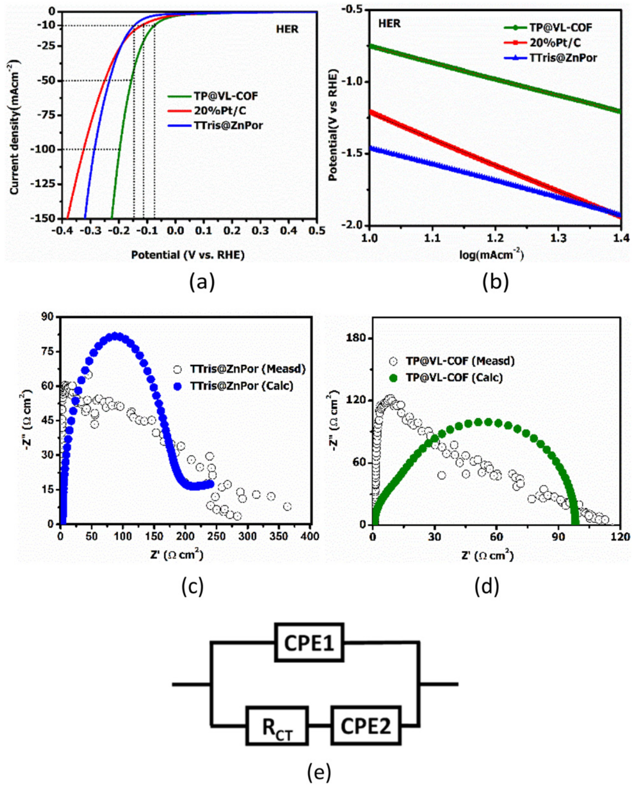

(a) (b)

(c) (d)

(e)

Fig. 7 Electrocatalysis observations of 20%Pt/C, TTris@ZnPor and TP@VL-COF in an alkaline medium (1 M KOH) at a scan rate of 10 mV s^{-1}. (a) LSV curves for the HER. (b) Tafel plots for the HER. Nyquist EIS plots for (c) TTris@ZnPor and (d) TP@VL-COF. (e) EIS equivalent circuit for both TTris@ZnPor and TP@VL-COF.

Table 2 HER overpotential and Tafel slope data for 20%Pt/C, TP@VL-COF, TTris@ZnPor and Lindqvist POM

	Overpotential (mV)				
Catalysts	At 10, mA cm^{-2}	At 50, mA cm^{-2}	At 100, mA cm^{-2}	Tafel slope (mV dec^{-1})	Ref.
TP@VL-COF	75	155	197	114	
20%Pt/C	113	250	324	182	
TTris@ZnPor	146	234	286	116	
Lindqvist POM	105	193	250	125	
NiTAPP-NiACQ	117				120
NiTAPP-ACQ	240				120
CoCOP	310				121
rGO-Fe_3O_4	310				122
$CoMoS_4$	256				123
PyCoPc/GO	253				124
NiFeSe/CFP	186				125
N@Mo2C-2/CFP	91				126
N@Mo2C-3/CFP	56				126
NiMo6O24@Cu/TNA	130				127

which accounts for the significantly reduced impedance of TP@VL-COF.

EIS of the synthesized organic and inorganic framework TP@VL-COF along with its precursor TTris@ZnPor was executed at 0.2 V in the frequency window of 0.1 Hz to 100 kHz with an amplitude of 5 mV *vs.* Ag/AgCl, and the Nyquist plots between ohmic *Z*′ (real impedance) and capacitive *Z*″ (imaginary impedance) are shown in Fig. 7(c) and 7(d). The charge transfer resistance (R_{ct}) between the electrode and electrolyte is indicated by semi-circles. The solution resistance, constant phase elements (CPEs), capacitance and charge transfer resistance at the interface between the electrolyte and the electrode surface in the high-frequency region are calculated and presented in Table 3. CPE parameters correspond to the bilayer behaviour of the electrocatalytic material, describing the impendence circuit's formulation. R_{ct}, R_s and the best-fitted circuit diagram are produced using ZSimpWin software. TP@VL-COF (Fig. 7d) and TTris@ZnPor (Fig. 7c) showed 98 Ω, and 201 Ω R_{ct}, respectively. It is actually the electron transfer hindrance between atoms of the electrolyte and the electrode measured electrochemically; therefore, an electrode catalyst that has a low value of R_{ct} is the best electrocatalyst. From the observed findings, it can be seen that TP@VL-COF also has a lower R_{ct} as compared to 20%Pt/C that also contains a metal part in its composition. In some systems, the Nyquist plot (also called the Cole–Cole plot or complex impedance plane plot) was expected to be a semicircle with the centre on the *x*-axis. Macdonald[112] points out that even though a particular theory may not exactly predict the CPE behaviour, it very often fits experimental data so well that the deviations are totally masked by experimental noise and uncertainties. This becomes increasingly true as the complexity of a circuit model increases. In short, a CPE can provide a useful modelling element, even if the true nature of the system is unknown. The electrochemical stability of TP@VL-COF was analysed through the chronoamperometric technique in 1 M KOH solution for 20 hours at a constant potential of 0.6 V *vs.* Ag/AgCl, as shown in Fig. 8. The catalytic activity of TP@VL-COF was compared with a commercially purchased 20%Pt carbon hybrid. It is very well known that the 20%Pt carbon hybrid is not good in alkaline media; here in alkaline media TP@VL-COF showed excellent reductive fuel generation activity in terms of overpotential and Tafel slope in comparison to 20%Pt/C. However, the stability of TP@VL-COF is not excellent, it showed a current loss of 17% for a time period of 20 hours, our compound contains a gigantic covalent framework which possesses numerous covalent bonds that showed inherent resistive capability, but

Table 3 EIS parameters of TP@VL-COF, TTris@ZnPor and 20%Pt/C

Parameters↓/Sample→		TP@VL-COF	20%Pt/C	TTris@ZnPor
R_s (Ω cm^2)		1.06	1.04	24.6
C (μF)		5.23	38.71	0.24
R_{ct} (Ω cm^2)		98	456.47	201
CPEs (μS sn cm^{-2})	Y	2.13	84.49	0.0051
	N	0.2878	0.71	0.08

"Y" indicates presence of Constant Phase Element (CPE) behavior in electrochemical system, while "N" quantifies its non-ideality or dispersion, with lower values suggesting greater deviation from ideal behavior.

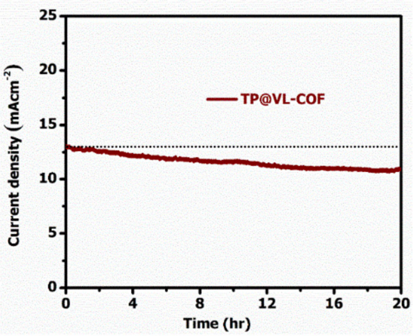

Fig. 8 Stability analysis of the electrode (TP@VL-COF) using the chronoamperometric technique in 1 M KOH *vs.* Ag/AgCl.

retaining current up to 83% with covalent bonding is encouraging.

The Lindqvist POM cluster can take up more chemical intermediates, which improves the kinetics of the HER. Actually, the active ingredient is primarily responsible for the electrocatalytic activity. The strength of hydrogen intermediate adsorption on the catalyst and the dissociation of water has an impact on the electroactivity in an alkaline electrolyte. The surface of the Lindqvist POM cluster in TP@VL-COF was found to be the active site in this investigation. This characteristic makes it possible to absorb more chemical intermediates, which improves the adsorption process for water molecules and increases the HER kinetics. By improving the kinetics of the HER, charge transfer is improved.[113–115] Furthermore, an overall increase in electrocatalytic activity was facilitated by the synergistic effects of the catalytic efficiency of metalloporphyrins coordinated in their backbone.[116,117]

The anodic oxidation of H_2O or OH^- and the cathodic reduction of H_2O or H^+ are the two half-cell processes that make up the water splitting process. The number of H^+ and OH^- ions in the aqueous solution determines the particular cathodic and anodic processes.[118]

Based on the results of these studies, a HER mechanism has been developed. The use of the Heyrovsky (eqn (6)), Volmer (eqn (7)) and Tafel (eqn (8)) techniques can provide insight into the HER mechanism of the reductive half-reaction in alkaline medium.[119] The initial stage is usually represented by the discharge reaction, sometimes referred to as the Volmer step. Either the combination process (Tafel step) or the ion–atom reaction (Heyrovsky step) ultimately produces hydrogen.

$$M + H_2O + e^- \rightarrow M - H* + OH^- \tag{6}$$

$$H_2O + e^- + M - H* \rightarrow M + H_2 + OH^- \tag{7}$$

$$M - H* + M - H* \rightarrow 2M + H_2 \tag{8}$$

Overall, the reaction is:

$$2H_2O + 2e^- \rightarrow H_2 + 2OH^- \tag{9}$$

where M = TTris@ZnPor and TP@VL-COF, respectively.

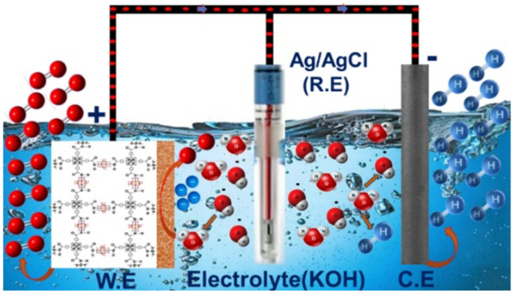

Fig. 9 Pictorial representation of the electrocatalytic HER mechanism at the surface of the TP@VL-COF.

The TP@VL-COF component TTris@ZnPor provides active catalytic sites for the HER. Throughout the HER process, the metalloporphyrin moiety facilitates electron transport as a redox-active core. Moreover, the porphyrin structure supplies coordination sites for proton binding, facilitating the initial adsorption of hydrogen ions (H^+) onto the COF surface. Conversely, the Lindqvist POM redox properties contribute to an increase in the overall catalytic activity. The POM cluster acts as an electron transfer mediator, facilitating the flow of electrons (e^-) between the metalloporphyrin sites and the electrolyte during the HER. It was predicted that V(v) would be reduced to V(iv) for TP@VL-COF during the hydrogen evolution process, causing changes in the electronic structures of TP@VL-COF. As a result, upon receiving electrons, HER active species such as V(iv)–H* intermediates would be generated. These intermediaries would eventually take up electrons at the surface of the formed systems, resulting in the production of H_2 molecules (Fig. 9).

Zn is necessary for the stability of the porphyrin core in the TTris@ZnPor since Zn(ii) is inactive for HER because of the d^{10} system.[128] The trisfucntionalized groups and the metalloporphyrin core facilitate the electron transfer and adsorption of hydrogen ions (H^+). Furthermore, reactive intermediates implicated in the HER process are more stable when POM clusters are present. The combined catalytic qualities of both components (TTris@ZnPor and Lindqvist POM) produce the synergistic catalytic reduction effect of TP@VL-COF. Lindqvist POM supplies inorganic polyoxometalate clusters with redox potential, while TTris@ZnPor supplies organic ligands with catalytic activity. Compared to the individual components, this synergistic combination produced greater catalytic performance by enabling more catalytic routes, improved substrate binding, and increased the stability of reaction intermediates.

5. Conclusion

To summarize, we developed TP@VL-COF, a new electrocatalyst generated from the covalent linkage of TTris@ZnPor and Lindqvist POM. TP@VL-COF performs very well in the HER in an alkaline electrolyte, with a lower overpotential of 75 mV at 10 mA cm^{-2} and quick kinetics with 25 mV dec^{-1} Tafel slope value. TP@VL-COF provides a new framework for creating synthesizable nonprecious electrocatalysts with efficient activity and durability in the HER using metal ions as active sites. This research opens the door to further investigation of various porphyrin and POM-derived conductive conjugated polymerized frameworks in electrochemical energy and water splitting systems. With great potential for use in renewable energy applications, covalent organic frameworks can provide novel ways to modify a material's electrocatalytic characteristics.

Author contributions

The manuscript was written through contributions of all authors. All authors have given approval to the final version of the manuscript. Sonia Rani: conceptualization, experimental design, methodology, manuscript composition, data curation, and software. Mazen R. Alrahili: software. Marwan Shalash: software. Moazzam H. Bhatti: software. Muhammad Nadeem: characterization and validation. Khurram Shahzad Munawar: software. Muhammad Tariq: investigation and supervision. Hafiz Muhammad Asif: visualization, investigation, and supervision. Zeinhom M. El-Bahy: software.

Conflicts of interest

The authors declare that they have no known competing financial interests or personal relationships that could have appeared to influence the work reported in the article.

Acknowledgements

The authors extend their appreciation to the Deanship of Scientific Research at Northern Border University, Arar, KSA for funding this research work through the project number "NBU-FFR-2024-2885-04". The authors are grateful for the financial support of the Bahauddin Zakariya University, Multan under project D-No.ORIC/2022/166, Pakistan. The authors are also grateful to their respective universities for providing the conducive environment for this work.

References

1 B. M. Hunter, H. B. Gray and A. M. Muller, Earth-abundant heterogeneous water oxidation catalysts, *Chem. Rev.*, 2016, **116**(22), 14120–14136.

2 N. S. Lewis and D. G. Nocera, Powering the planet: Chemical challenges in solar energy utilization, *Proc. Natl. Acad. Sci. U. S. A.*, 2006, **103**(43), 15729–15735.

3 M. D. Savage, *Global Energy Consumption: An Analysis of Variables That Shape Per Capita Usage, or How Pump Price, Urbanization, and Fossil Fuels Imports Impact Fossil Fuels Consumption Per Capita Across OECD Countries*, Old Dominion University, 2023, pp. 30634141.

4 L. Jiao, X. Zhang, Y. Feng, J. Lin, D. Yuan and Y. Wang, Coupled Solar Battery with 6.9% Efficiency, *Angew. Chem.*, 2023, e202306506.

5 C.-F. Li, H.-B. Tang, J.-W. Zhao and G.-R. Li, Constructing Fe/Ni atomic interfaces in Fe-doped Ni $(OH)_2$ with single-phase structures for efficient oxygen evolution, *J. Mater. Chem. A*, 2023, **11**(11), 5841–5850.

6 J. Wang, Y. Ren and P. Wang, (Fe, F) co-doped nickel oxyhydroxide for highly efficient oxygen evolution reaction, *J. Mater. Chem. A*, 2023, **11**(9), 4619–4626.

7 S. Chu and A. Majumdar, Opportunities and challenges for a sustainable energy future, *Nature*, 2012, **488**(7411), 294–303.

8 B. You and Y. Sun, Innovative strategies for electrocatalytic water splitting, *Acc. Chem. Res.*, 2018, **51**(7), 1571–1580.

9 J. E. G. Baquero and D. B. Monsalve, From fossil fuel energy to hydrogen energy: Transformation of fossil fuel energy economies into hydrogen economies through social entrepreneurship, *Int. J. Hydrogen Energy*, 2023, **54**, 574–585.

10 E. Boateng, A. R. Thiruppathi, C.-K. Hung, D. Chow, D. Sridhar and A. Chen, Functionalization of graphene-based nanomaterials for energy and hydrogen storage, *Electrochim. Acta*, 2023, **452**, 142340.

11 J. Guo, W. Liu, X.-C. Fu and S. Jiao, Wet-chemistry synthesis of two-dimensional Pt-and Pd-based intermetallic electrocatalysts for fuel cells, *Nanoscale*, 2023, **15**, 6545–6553.

12 C. L. Vecchio, Innovative Electrocatalysts for Fuel Cell and Battery Applications, *Catalysts*, 2023, **13**(2), 359.

13 L. Ni, J. Gu, X. Jiang, H. Xu, Z. Wu, Y. Wu, Y. Liu, J. Xie, Y. Wei and G. Diao, Polyoxometalate–Cyclodextrin–Based Cluster–Organic Supramolecular Framework for Polysulfide Conversion and Guest–Host Recognition in Lithium–sulfur Batteries, *Angew. Chem.*, 2023, **135**(36), e202306528.

14 L. Li, P. Wang, Q. Shao and X. Huang, Recent progress in advanced electrocatalyst design for acidic oxygen evolution reaction, *Adv. Mater.*, 2021, **33**(50), 2004243.

15 C. C. McCrory, S. Jung, I. M. Ferrer, S. M. Chatman, J. C. Peters and T. F. Jaramillo, Benchmarking hydrogen evolving reaction and oxygen evolving reaction electrocatalysts for solar water splitting devices, *J. Am. Chem. Soc.*, 2015, **137**(13), 4347–4357.

16 Z. Wan, Z. Ma, H. Yuan, K. Liu and X. Wang, Sulfur engineering on NiFe layered double hydroxide at ambient temperature for high current density oxygen evolution reaction, *ACS Appl. Energy Mater.*, 2022, **5**(4), 4603–4612.

17 M. R. Horn, A. Singh, S. Alomari, S. Goberna-Ferrón, R. Benages-Vilau, N. Chodankar, N. Motta, K. K. Ostrikov, J. MacLeod and P. Sonar, Polyoxometalates (POMs): from electroactive clusters to energy materials, *Energy Environ. Sci.*, 2021, **14**(4), 1652–1700.

18 C. Freire, D. M. Fernandes, M. Nunes and V. K. Abdelkader, POM & MOF–based Electrocatalysts for Energy–related Reactions, *ChemCatChem*, 2018, **10**(8), 1703–1730.

19 N. Lv, Q. Li, H. Zhu, S. Mu, X. Luo, X. Ren, X. Liu, S. Li, C. Cheng and T. Ma, Electrocatalytic Porphyrin/Phthalocyanine–Based Organic Frameworks: Building Blocks, Coordination Microenvironments, Structure–Performance Relationships, *Adv. Sci.*, 2023, **10**(7), 2206239.

20 H.-g. Wang, Q. Wu, L. Cheng, L. Chen, M. Li and G. Zhu, Porphyrin-and phthalocyanine-based systems for rechargeable batteries, *Energy Storage Mater.*, 2022, **52**, 427–450.

21 S.-W. Ke, W. Li, Y. Gu, J. Su, Y. Liu, S. Yuan, J.-L. Zuo, J. Ma and P. He, Covalent organic frameworks with Ni-Bis (dithiolene) and Co-porphyrin units as bifunctional catalysts for Li-O_2 batteries, *Sci. Adv.*, 2023, **9**(5), eadf2398.

22 J. Tang, T. Liu, S. Miao and Y. Cho, Emerging energy harvesting technology for electro/photo-catalytic water splitting application, *Catalysts*, 2021, **11**(1), 142.

23 S. Wang, Y. Zhang, X. Deng, Z. Ma, H. Yuan, J. Li and X. Wang, Metal-organic framework derived ellipse-like NiS_2 nanocatalyst for stable electrochemical hydrogen generation in alkaline electrolyte, *Int. J. Hydrogen Energy*, 2022, **47**(97), 40932–40942.

24 T. Li and W. Hu, Ionic Liquid Derived Electrocatalysts for Electrochemical Water Splitting, *Green Energy Environ.*, 2024, **9**(4), 604–622.

25 T. Zhu, J. Han, T. Sun, J. Chen, S. Wang, S. Ren, X. Pi, J. Xu and K. Chen, Interface-Enhanced SiO_x/Ru Heterocatalysts for Efficient Electrochemical Water Splitting, *ACS Appl. Mater. Interfaces*, 2023, **15**(6), 8200–8207.

26 G. He and Y. Liao, Modification of micro/nanoscaled manganese dioxide-based materials and their electrocatalytic applications toward oxygen evolution reaction, *J. Mater. Chem. A*, 2023, **11**, 6688–6746.

27 N. Attarzadeh, D. Das, S. N. Chintalapalle, S. Tan, V. Shutthanandan and C. Ramana, Nature-Inspired Design of Nano-Architecture-Aligned Ni5P4-Ni2P/NiS Arrays for Enhanced Electrocatalytic Activity of Hydrogen Evolution Reaction (HER), *ACS Appl. Mater. Interfaces*, 2023, **15**(18), 22036–22050.

28 X. Zhu, L. Chen, Y. Liu and Z. Tang, Atomically precise Au nanoclusters for electrochemical hydrogen evolution catalysis: Progress and perspectives, *Polyoxometalates*, 2023, **2**(4), 9140031.

29 Z. Duan, X. Tan, Y. Sun, W.-C. Zhang, A. Umar and X. Wu, Manipulating the electrocatalytic performance of NiCoP nanowires by V doping under acidic and basic conditions for hydrogen and oxygen evolution reactions, *ACS Appl. Nano Mater.*, 2021, **4**(10), 10791–10798.

30 Z. Zang, X. Wang, X. Li, Q. Zhao, L. Li, X. Yang, X. Yu, X. Zhang and Z. Lu, Co_9S_8 nanosheet coupled Cu2S nanorod heterostructure as efficient catalyst for overall water splitting, *ACS Appl. Mater. Interfaces*, 2021, **13**(8), 9865–9874.

31 N. Nie, D. Zhang, Z. Wang, Y. Qin, X. Zhai, B. Yang, J. Lai and L. Wang, Superfast Synthesis of Densely Packed and Ultrafine Pt–Lanthanide@ KB via Solvent–Free Microwave as Efficient Hydrogen Evolution Electrocatalysts, *Small*, 2021, **17**(36), 2102879.

32 X. Fan, C. Liu, B. Gao, H. Li, Y. Zhang, H. Zhang, Q. Gao, X. Cao and Y. Tang, Electronic Structure Engineering of Pt Species over Pt/WO_3 toward Highly Efficient Electrocatalytic Hydrogen Evolution, *Small*, 2023, 2301178.

33 X. Ren, Q. Lv, L. Liu, B. Liu, Y. Wang, A. Liu and G. Wu, Current progress of Pt and Pt-based electrocatalysts used for fuel cells, *Sustainable Energy Fuels*, 2020, **4**(1), 15–30.

34 D. Li, C. Wang, D. S. Strmcnik, D. V. Tripkovic, X. Sun, Y. Kang, M. Chi, J. D. Snyder, D. van der Vliet and Y. Tsai, Functional links between Pt single crystal morphology and nanoparticles with different size and shape: the oxygen reduction reaction case, *Energy Environ. Sci.*, 2014, **7**(12), 4061–4069.

35 G. Andreadis and P. Tsiakaras, Ethanol crossover and direct ethanol PEM fuel cell performance modeling and experimental validation, *Chem. Eng. Sci.*, 2006, **61**(22), 7497–7508.

36 Y. Hao, X. Wang, J. Shen, J. Yuan, A.-J. Wang, L. Niu and S. Huang, One-pot synthesis of single-crystal Pt nanoplates uniformly deposited on reduced graphene oxide, and their high activity and stability on the electrocalalytic oxidation of methanol, *Nanotechnology*, 2016, **27**(14), 145602.

37 H. Lv and S. Mu, Nano-ceramic support materials for low temperature fuel cell catalysts, *Nanoscale*, 2014, **6**(10), 5063–5074.

38 K. Y. Cho, Y. S. Yeom, H. Y. Seo, A. S. Lee, X. H. Do, J. P. Hong, H.-K. Jeong, K.-Y. Baek and H. G. Yoon, Fine-sized Pt nanoparticles dispersed on PdPt bimetallic nanocrystals with non-covalently functionalized graphene toward synergistic effects on the oxygen reduction reaction, *Electrochim. Acta*, 2017, **257**, 412–422.

39 Y. Wang, Y. Lu, W. Zhang, T. Dang, Y. Yang, X. Bai and S. Liu, Construction of hydrogel composites with superior proton conduction and flexibility using a new POM-based inorganic–organic hybrid, *Polyoxometalates*, 2022, **1**(1), 9140005.

40 D. Zang and H. Wang, Polyoxometalate-based nanostructures for electrocatalytic and photocatalytic CO 2 reduction, *Polyoxometalates*, 2022, **1**(1), 9140006.

41 H.-Y. Zhao, Y.-Z. Li, J.-W. Zhao, L. Wang and G.-Y. Yang, State-of-the-art advances in the structural diversities and catalytic applications of polyoxoniobate-based materials, *Coord. Chem. Rev.*, 2021, **443**, 213966.

42 Z. Zeb, Y. Huang, L. Chen, W. Zhou, M. Liao, Y. Jiang, H. Li, L. Wang, L. Wang and H. Wang, Comprehensive overview of polyoxometalates for electrocatalytic hydrogen evolution reaction, *Coord. Chem. Rev.*, 2023, **482**, 215058.

43 A. Yokoyama, T. Kojima, K. Ohkubo and S. Fukuzumi, A discrete conglomerate of a distorted Mo(V)-porphyrin with a directly coordinated keggin-type polyoxometalate, *Chem. Commun.*, 2007, (39), 3997–3999.

44 D. Attanasio and F. Bachechi, Weak ternary CT salts formed by α–keggin polyanions and tetraphenylporphyrinato ZnII in the presence of halide ions, *Adv. Mater.*, 1994, **6**(2), 145–147.

45 D. Hagrman, P. J. Hagrman and J. Zubieta, Solid–state coordination chemistry: the self–assembly of microporous organic–inorganic hybrid frameworks constructed from tetrapyridylporphyrin and bimetallic oxide chains or oxide clusters, *Angew. Chem., Int. Ed.*, 1999, **38**(21), 3165–3168.

46 A. Tsuda, E. Hirahara, Y. S. Kim, H. Tanaka, T. Kawai and T. Aida, A molybdenum crown cluster forms discrete inorganic–organic nanocomposites with metalloporphyrins, *Angew. Chem., Int. Ed.*, 2004, **43**(46), 6327–6331.

47 S.-Q. Liu, J.-Q. Xu, H.-R. Sun and D.-M. Li, meso-Tetrakis (4-N-benzylpyridyl) porphyrin and its supramolecular complexes formed with anionic metal–oxo cluster: spectroscopy and electrocatalytic reduction of dioxygen, *Inorg. Chim. Acta*, 2000, **306**(1), 87–93.

48 I. C. Santos, S. L. Rebelo, M. S. S. Balula, R. R. Martins, M. M. M. Pereira, M. M. Simões, M. G. P. Neves, J. A. Cavaleiro and A. M. Cavaleiro, Association of Keggin-type anions with cationic meso-substituted porphyrins: synthesis, characterization and oxidative catalytic studies, *J. Mol. Catal. A: Chem.*, 2005, **231**(1–2), 35–45.

49 Y. Zhang, S. Chen, Y. Zhang, R. Li, B. Zhao and T. Peng, Hydrogen–Bond Regulation of the Microenvironment of Ni(II)–Porphyrin Bifunctional Electrocatalysts for Efficient Overall Water Splitting, *Adv. Mater.*, 2023, 2210727.

50 X. Peng, J. Han, X. Li, G. Liu, Y. Xu, Y. Peng, S. Nie, W. Li, X. Li and Z. Chen, Electrocatalytic hydrogen evolution with a copper porphyrin bearing meso-(o-carborane) substituents, *Chem. Commun.*, 2023, **59**(72), 10777–10780.

51 Y. Dou, A. Wang, L. Zhao, X. Yang, Q. Wang, M. S. Sudi, W. Zhu and D. Shang, Boosted hydrogen evolution reaction for a nitrogen-rich azo-bridged metallated porphyrin network, *J. Colloid Interface Sci.*, 2023, **650**, 943–950.

52 S. Li, J. Li, H. Zhu, L. Zhang, X. Sang, Z. Zhu, W. You and F. Zhang, Development of polyoxometalate-based Ag-H_2 biim inorganic–organic hybrid compounds functionalized for the acid electrocatalytic hydrogen evolution reaction, *Dalton Trans.*, 2023, **52**(43), 15725–15733.

53 H. Jia, Y. Yao, Y. Gao, D. Lu and P. Du, Pyrolyzed cobalt porphyrin-based conjugated mesoporous polymers as bifunctional catalysts for hydrogen production and oxygen evolution in water, *Chem. Commun.*, 2016, **52**(92), 13483–13486.

54 L. Jiao, Y.-X. Zhou and H.-L. Jiang, Metal–organic framework-based CoP/reduced graphene oxide: high-performance bifunctional electrocatalyst for overall water splitting, *Chem. Sci.*, 2016, **7**(3), 1690–1695.

55 Y. Zhang, Y. Liu, D. Wang, J. Liu, J. Zhao and L. Chen, State-of-the-art advances in the syntheses, structures, and applications of polyoxometalate-based metal–organic frameworks, *Polyoxometalates*, 2023, **2**(1), 9140017.

56 Y. An, L. Wang, W. Jiang, X. Lv, G. Yuan, X. Hang and H. Pang, Metal–organic framework-based materials for photocatalytic overall water splitting: Status and prospects, *Polyoxometalates*, 2023, **2**(3), 9140030.

57 S. Bhunia, K. Bhunia, B. C. Patra, S. K. Das, D. Pradhan, A. Bhaumik, A. Pradhan and S. Bhattacharya, Efficacious electrochemical oxygen evolution from a novel Co(II) porphyrin/pyrene-based conjugated microporous polymer, *ACS Appl. Mater. Interfaces*, 2018, **11**(1), 1520–1528.

58 H. B. Aiyappa, J. Thote, D. B. Shinde, R. Banerjee and S. Kurungot, Cobalt-modified covalent organic framework as a robust water oxidation electrocatalyst, *Chem. Mater.*, 2016, **28**(12), 4375–4379.

59 C. R. Mulzer, L. Shen, R. P. Bisbey, J. R. McKone, N. Zhang, H. D. Abruña and W. R. Dichtel, Superior charge storage and power density of a conducting polymer-modified covalent organic framework, *ACS Cent. Sci.*, 2016, **2**(9), 667–673.

60 V. Sharma, M. Nemiwal and D. Kumar, Catalytic applications of recent and improved covalent organic frameworks, *Mini-Rev. Org. Chem.*, 2022, **19**(7), 815–825.

61 W. K. Haug, E. R. Wolfson, B. T. Morman, C. M. Thomas and P. L. McGrier, A nickel-doped dehydrobenzoannulene-based two-dimensional covalent organic framework for the reductive cleavage of inert aryl C–S bonds, *J. Am. Chem. Soc.*, 2020, **142**(12), 5521–5525.

62 S. Yan, X. Guan, H. Li, D. Li, M. Xue, Y. Yan, V. Valtchev, S. Qiu and Q. Fang, Three-dimensional salphen-based covalent–organic frameworks as catalytic antioxidants, *J. Am. Chem. Soc.*, 2019, **141**(7), 2920–2924.

63 S. Cui, M. Qian, X. Liu, Z. Sun and P. Du, A Copper Porphyrin–Based Conjugated Mesoporous Polymer–Derived Bifunctional Electrocatalyst for Hydrogen and Oxygen Evolution, *ChemSusChem*, 2016, **9**(17), 2365–2373.

64 K. S. Bhat, H. C. Barshilia and H. Nagaraja, Porous nickel telluride nanostructures as bifunctional electrocatalyst towards hydrogen and oxygen evolution reaction, *Int. J. Hydrogen Energy*, 2017, **42**(39), 24645–24655.

65 T. Nakagawa, N. S. Bjorge and R. W. Murray, Electrogenerated IrO_x nanoparticles as dissolved redox catalysts for water oxidation, *J. Am. Chem. Soc.*, 2009, **131**(43), 15578–15579.

66 Y. V. Geletii, B. Botar, P. Kogerler, D. A. Hillesheim, D. G. Musaev and C. L. Hill, An all-inorganic, stable, and highly active tetraruthenium homogeneous catalyst for water oxidation, *Angew. Chem.*, 2008, **120**(21), 3960.

67 O. Popovski, Electrocatalysts in the last 30 years–from precious metals to cheaper but sophisticated complex systems, *Bull. Chem. Technol. Maced.*, 2004, **23**(2), 101–112.

68 A. s. M. Ramírez, S. Heidari, A. Vergara, M. V. a. Aguilera, P. Preuss, M. B. Camarada and A. Fischer, Rhenium-Based Electrocatalysts for Water Splitting, *ACS Mater. Au*, 2023, **3**(3), 177–200.

69 S. Sun, H. Li and Z. J. Xu, Impact of surface area in evaluation of catalyst activity, *Joule*, 2018, **2**(6), 1024–1027.

70 G. Fu, X. Yan, Y. Chen, L. Xu, D. Sun, J. M. Lee and Y. Tang, Boosting bifunctional oxygen electrocatalysis with 3D graphene aerogel–supported Ni/MnO particles, *Adv. Mater.*, 2018, **30**(5), 1704609–1704000.

71 V. Jose, H. Hu, E. Edison, W. Manalastas Jr, H. Ren, P. Kidkhunthod, S. Sreejith, A. Jayakumar, J. M. V. Nsanzimana and M. Srinivasan, Modulation of single atomic Co and Fe sites on hollow carbon nanospheres as oxygen electrodes for rechargeable Zn–air batteries, *Small Methods*, 2021, **5**(2), 2000751.

72 K. S. Exner and H. Over, Kinetics of electrocatalytic reactions from first-principles: a critical comparison with the ab initio thermodynamics approach, *Acc. Chem. Res.*, 2017, **50**(5), 1240–1247.

73 Z. He, Y. Huang, A. K. Manohar and F. Mansfeld, Effect of electrolyte pH on the rate of the anodic and cathodic reactions in an air-cathode microbial fuel cell, *Bioelectrochemistry*, 2008, **74**(1), 78–82.

74 H. Wang, W. Zhang, X. Zhang, S. Hu, Z. Zhang, W. Zhou and H. Liu, Multi-interface collaboration of graphene cross-linked NiS-NiS 2-Ni 3 S 4 polymorph foam towards robust hydrogen evolution in alkaline electrolyte, *Nano Res.*, 2021, **14**, 4857–4864.

75 M. Liu, H. Li, S. Liu, L. Wang, L. Xie, Z. Zhuang, C. Sun, J. Wang, M. Tang and S. Sun, Tailoring activation sites of metastable distorted 1T′-phase MoS_2 by Ni doping for enhanced hydrogen evolution, *Nano Res.*, 2022, **15**(7), 5946–5952.

76 X.-P. Li, C. Huang, W.-K. Han, T. Ouyang and Z.-Q. Liu, Transition metal-based electrocatalysts for overall water splitting, *Chin. Chem. Lett.*, 2021, **32**(9), 2597–2616.

77 J. Zhou, F. Wang, H. Wang, S. Hu, W. Zhou and H. Liu, Ferrocene-induced switchable preparation of metal-nonmetal codoped tungsten nitride and carbide nanoarrays for electrocatalytic HER in alkaline and acid media, *Nano Res.*, 2023, **16**(2), 2085–2093.

78 C. Coutanceau, L. Demarconnay, C. Lamy and J.-M. Léger, Development of electrocatalysts for solid alkaline fuel cell (SAFC), *J. Power Sources*, 2006, **156**(1), 14–19.

79 W. Ma, X. Zhang, W. Li, M. Jiao, L. Zhang, R. Ma and Z. Zhou, Advanced Pt-based electrocatalysts for hydrogen evolution reaction in an alkaline medium, *Nanoscale*, 2023, **15**, 11759–11776.

80 B. V. Day, W. Klemperer and D. Maltbie, Where are the protons in $H_3V_{10}O_{283}$-?, *J. Am. Chem. Soc.*, 1987, **109**(10), 2991–3002.

81 Y. Zhu, Y. Huang, Q. Li, D. Zang, J. Gu, Y. Tang and Y. Wei, Polyoxometalate-based photoactive hybrid: uncover the first crystal structure of covalently linked hexavanadate-porphyrin molecule, *Inorg. Chem.*, 2020, **59**(4), 2575–2583.

82 S. Rani, M. Tariq, M. H. Bhatti, S. A. Abdelmohsen, M. M. Alanazi, M. A. Khan, H. M. Asif, M. Nadeem and R. Khan, A simplistic approach for the synthesis of Covalent Organic Frameworks (COFs) comprising of tetrafunctionalized porphyrin and polyoxometalates to uncover catalytic applications, *Opt. Mater.*, 2023, **138**, 113672.

83 B. Huang, Y. Wang, Z. Xiao, D. Ke, M. Cheng and P. Wu, A New Family of Polyoxometalates: Tris-functionalized Lindqvist-Type Hexatungstovanadates, *Inorg. Chem.*, 2021, **60**(2), 545–549.

84 C. E. Diaz-Uribe, A. Rodriguez, D. Utria, W. Vallejo, E. Puello, X. Zarate and E. Schott, Photocatalytic degradation of methylene blue by the Anderson-type polyoxomolybdates/TiO_2 thin films, *Polyhedron*, 2018, **149**, 163–170.

85 R. L. Frost, K. L. Erickson, M. L. Weier and O. Carmody, Raman and infrared spectroscopy of selected vanadates, *Spectrochim. Acta, Part A*, 2005, **61**(5), 829–834.

86 U. Saleem, M. Tariq, M. Nadeem, S. Hussain, M. A. Khan, H. M. Asif, A. Hussain, G. A. Mersal and I. H. El Azab, Synthesis of photoactive Polyoxometalate-porphyrin hybrids to trigger the photocurrent by designing the ultrathin films, *Opt. Mater.*, 2022, **134**, 113005.

87 H. M. Asif, A. Iqbal, Y. Zhou, L. Zhang, T. Wang, M. I. U. Farooqi and R. Sun, Preparation, characterization and third order optical nonlinearities of looped covalently bonded Anderson-type polyoxometalate-porphyrin hybrids, *Dyes Pigm.*, 2021, **184**, 108758.

88 H. M. Asif, Y. Zhou, L. Zhang, N. Shaheen, D. Yang, J. Li, Y. Long, A. Iqbal and Y. Li, Covalent synthesis of two hybrids composed of dawson-type polyoxometalate and porphyrin with remarkable third-order optical Nonlinearities Reflecting the Effect of Polyoxometalates, *Inorg. Chem.*, 2017, **56**(16), 9436–9447.

89 C. Allain, D. Schaming, N. Karakostas, M. Erard, J.-P. Gisselbrecht, S. Sorgues, I. Lampre, L. Ruhlmann and B. Hasenknopf, Synthesis, electrochemical and photophysical properties of covalently linked porphyrin–polyoxometalates, *Dalton Trans.*, 2013, **42**(8), 2745–2754.

90 U. Saleem, M. Tariq, M. Nadeem, S. Hussain, M. A. Khan, H. M. Asif, A. Hussain, G. A. Mersal and I. H. El Azab, Synthesis of photoactive Polyoxometalate-porphyrin hybrids to trigger the photocurrent by designing the ultrathin films, *Opt. Mater.*, 2022, **134**, 113005.

91 A. Mushtaq, M. Nadeem, I. A. Shaaban, M. A. Assiri, M. Sajid, M. A. Khan, H. M. Asif, Z. Nazar, S. Hussain and Z. M. El-Bahy, Catalytic oxidative desulfurization of thiocompounds by employing χ-Anderson-type polyoxometalates-porphyrin covalent organic framework (COF), *Tetrahedron*, 2023, 133575.

92 H. M. Asif, Y. Zhou, L. Zhang, N. Shaheen, D. Yang, J. Li, Y. Long, A. Iqbal and Y. Li, Covalent synthesis of two hybrids composed of dawson-type polyoxometalate and porphyrin with remarkable third-order optical Nonlinearities Reflecting the Effect of Polyoxometalates, *Inorg. Chem.*, 2017, **56**(16), 9436–9447.

93 Y. Zhu, Y. Huang, Q. Li, D. Zang, J. Gu, Y. Tang and Y. Wei, Polyoxometalate-based photoactive hybrid:

uncover the first crystal structure of covalently linked hexavanadate-porphyrin molecule, *Inorg. Chem.*, 2020, **59**(4), 2575–2583.

94 S. Chang, W. Xie, C. Yao, G. Xu, S. Zhang, Y. Xu and X. Ding, Construction of 2D porphyrin-based covalent organic framework as adsorbent for organic dyes removal and carbon dioxide adsorption, *J. Solid State Chem.*, 2021, **304**, 122577.

95 S. Kandambeth, D. B. Shinde, M. K. Panda, B. Lukose, T. Heine and R. Banerjee, Enhancement of chemical stability and crystallinity in porphyrin–containing covalent organic frameworks by intramolecular hydrogen bonds, *Angew. Chem.*, 2013, **125**(49), 13290–13294.

96 S. Abednatanzi, K. Leus, P. G. Derakhshandeh, F. Nahra, K. De Keukeleere, K. Van Hecke, I. Van Driessche, A. Abbasi, S. P. Nolan and P. Van Der Voort, POM@IL-MOFs–inclusion of POMs in ionic liquid modified MOFs to produce recyclable oxidation catalysts, *Catal. Sci. Technol.*, 2017, **7**(7), 1478–1487.

97 S. Bag and S. Bhowmik, Fluorescence Spectroscopy: A Useful Method to Explore the Interactions of Small Molecule Ligands with DNA Structures, in *Reverse Engineering of Regulatory Networks*, Springer, 2023, pp. 33–49.

98 S. G. Schulman, *Fluorescence and phosphorescence spectroscopy: physicochemical principles and practice*, Elsevier, 2017, pp. 293.

99 Z.-D. Yan, L.-D. Sun, C.-G. Hu, X.-T. Hu and Z. Peter, Factors influencing the ability of fluorescence emission and fluorescence quenching experimental research, *Spectrosc. Spectral Anal.*, 2012, **32**(10), 2718–2721.

100 A. Köhler, J. S. Wilson and R. H. Friend, Fluorescence and phosphorescence in organic materials, *Adv. Mater.*, 2002, **14**(10), 701–707.

101 A. Bose, I. Thomas and E. Abraham, Fluorescence spectroscopy and its applications: A Review, *Int. J. Adv. Pharm. Anal.*, 2018, **8**(1), 1–8.

102 S. K. Cushing, M. Li, F. Huang and N. Wu, Origin of strong excitation wavelength dependent fluorescence of graphene oxide, *ACS Nano*, 2014, **8**(1), 1002–1013.

103 M. Józefowicz and J. R. Heldt, Excitation-wavelength dependent fluorescence of ethyl 5-(4-aminophenyl)-3-amino-2, 4-dicyanobenzoate, *J. Fluoresc.*, 2011, **21**, 239–245.

104 K. Nawara and J. Waluk, Improved method of fluorescence quantum yield determination, *Anal. Chem.*, 2017, **89**(17), 8650–8655.

105 V. V. Zarubaev, T. C. Kris'ko, E. V. Kriukova and T. D. Muraviova, Effect of albumin on the fluorescence quantum yield of porphyrin-based agents for fluorescent diagnostics, *Photodiagn. Photodyn. Ther.*, 2017, **20**, 137–143.

106 F. Bokaei, R. Rahimi and M. Rabbani, Metalloporphyrin-based Ni/Co metal–organic framework: preparation, characterization and photodegradation of 1, 5-DHN, *Polym. Bull.*, 2024, 1–27.

107 H. Abudukeremu, N. Kari, Y. Zhang, J. Wang, P. Nizamidin, S. Abliz and A. Yimit, Highly sensitive free-base-porphyrin-based thin-film optical waveguide sensor for detection of low concentration NO_2 gas at ambient temperature, *J. Mater. Sci.*, 2018, **53**(15), 10822–10834.

108 S. Nadeem, M. I. A. Mutalib and M. Shima, One pot syntheses and characterization of meso-5, 10, 15, 20-copper tetraphenylporphyrin, *Rasayan J. Chem.*, 2016, **9**(3), 309–314.

109 A. Salker and S. Gokakakar, Solar assisted photo-catalytic degradation of Amido Black 10B over cobalt, nickel and zinc metalloporphyrins, *J. Phys. Sci.*, 2009, **4**, 377–384.

110 W. Zhang, W. Li, X. He, L. Zhao, H. Chen, L. Zhang, P. Tian, Z. Xin, W. Fang and F. Zhang, Dendritic Fe-based polyoxometalates@ metal–organic framework (MOFs) combined with ZnO as a novel photoanode in solar cells, *J. Mater. Sci.: Mater. Electron.*, 2018, **29**, 1623–1629.

111 W. Xu, X. Pei, C. S. Diercks, H. Lyu, Z. Ji and O. M. Yaghi, A metal–organic framework of organic vertices and polyoxometalate linkers as a solid-state electrolyte, *J. Am. Chem. Soc.*, 2019, **141**(44), 17522–17526.

112 J. R. Macdonald, Impedance spectroscopy and its use in analyzing the steady-state AC response of solid and liquid electrolytes, *J. Electroanal. Chem. Interfacial Electrochem.*, 1987, **223**(1–2), 25–50.

113 X.-L. Wang, Y. Tian, Z.-H. Chang and H. Lin, A series of polyoxometalate-based metal–bis (pyridyl-tetrazole) complexes with high electrocatalytic activity for hydrogen evolution reaction in alkaline and acid media, *ACS Sustainable Chem. Eng.*, 2020, **8**(41), 15696–15702.

114 Y.-J. Tang, A.-M. Zhang, H.-J. Zhu, L.-Z. Dong, X.-L. Wang, S.-L. Li, M. Han, X.-X. Xu and Y.-Q. Lan, Polyoxometalate precursors for precisely controlled synthesis of bimetallic sulfide heterostructure through nucleation-doping competition, *Nanoscale*, 2018, **10**(18), 8404–8412.

115 W. Luo, J. Hu, H. Diao, B. Schwarz, C. Streb and Y. F. Song, Robust polyoxometalate/nickel foam composite electrodes for sustained electrochemical oxygen evolution at high pH, *Angew. Chem., Int. Ed.*, 2017, **56**(18), 4941–4944.

116 S. Sohrabi, S. Dehghanpour and M. Ghalkhani, A cobalt porphyrin-based metal organic framework/multi-walled carbon nanotube composite electrocatalyst for oxygen reduction and evolution reactions, *J. Mater. Sci.*, 2018, **53**(5), 3624–3639.

117 A. Wang, L. Cheng, W. Zhao, X. Shen and W. Zhu, Electrochemical hydrogen and oxygen evolution reactions from a cobalt-porphyrin-based covalent organic polymer, *J. Colloid Interface Sci.*, 2020, **579**, 598–606.

118 O. Basu, S. Mukhopadhyay and S. K. Das, Cobalt based functional inorganic materials: Electrocatalytic water oxidation, *J. Chem. Sci.*, 2018, **130**, 1–15.

119 Z. Liang, H.-Y. Wang, H. Zheng, W. Zhang and R. Cao, Porphyrin-based frameworks for oxygen electrocatalysis and catalytic reduction of carbon dioxide, *Chem. Soc. Rev.*, 2021, **50**(4), 2540–2581.

120 A. Wang, X. Yang, Q. Wang, Y. Dou, L. Zhao, W. Zhu, W. Zhao and G. Zhu, Acenaphthenediimine complex-bridged porphyrin porous organic polymer with enriched active sites as a robust water splitting electrocatalyst, *J. Colloid Interface Sci.*, 2024, **657**, 748–756.

121 A. Wang, L. Cheng, W. Zhao, X. Shen and W. Zhu, Electrochemical hydrogen and oxygen evolution reactions from a cobalt-porphyrin-based covalent organic polymer, *J. Colloid Interface Sci.*, 2020, **579**, 598–606.

122 A. Hanan, M. Ahmed, M. N. Lakhan, A. H. Shar, D. Cao, A. Asif, A. Ali and M. Gul, Novel rGO@Fe3O4 nanostructures: An active electrocatalyst for hydrogen evolution reaction in alkaline media, *J. Indian Chem. Soc.*, 2022, **99**(5), 100442.

123 A. Yadav, Y. Hunge and S.-W. Kang, Highly efficient porous morphology of cobalt molybdenum sulfide for overall water splitting reaction, *Surf. Interfaces*, 2021, **23**, 101020.

124 L. Chen, R. U. R. Sagar, J. Chen, J. Liu, S. Aslam, F. Nosheen, T. Anwar, N. Hussain, X. Hou and T. Liang, Cobalt phthalocyanine as an efficient catalyst for hydrogen evolution reaction, *Int. J. Hydrogen Energy*, 2021, **46**(37), 19338–19346.

125 Y. Guo, Y. Liu, Y. Liu, C. Zhang, K. Jia, J. Su and K. Wang, The high electrocatalytic performance of NiFeSe/CFP for hydrogen evolution reaction derived from a prussian blue analogue, *Catalysts*, 2022, **12**(7), 739.

126 Y. Huang, J. Hu, H. Xu, W. Bian, J. Ge, D. Zang, D. Cheng, Y. Lv, C. Zhang and J. Gu, Fine tuning electronic structure of catalysts through atomic engineering for enhanced hydrogen evolution, *Adv. Energy Mater.*, 2018, **8**(24), 1800789.

127 D. Zang, Y. Huang, Q. Li, Y. Tang and Y. Wei, Cu dendrites induced by the Anderson-type polyoxometalate $NiMo_6O_{24}$ as a promising electrocatalyst for enhanced hydrogen evolution, *Appl. Catal., B*, 2019, **249**, 163–171.

128 H. M. Castro-Cruz and N. A. Macias-Ruvalcaba, Porphyrin-catalyzed electrochemical hydrogen evolution reaction. Metal-centered and ligand-centered mechanisms, *Coord. Chem. Rev.*, 2022, **458**, 214430.